Supporting Information

Type-printable photodetector arrays for multichannel meta-infrared imaging

Junxiong Guo[1,2,#,*], Shuyi Gu[1,#], Lin Lin[2,#], Yu Liu[3,4*], Ji Cai[1], Hongyi Cai[1], Yu Tian[5], Yuelin Zhang[5], Qinghua Zhang[6], Ze Liu[1], Yafei Zhang[1], Xiaosheng Zhang[2], Yuan Lin[2], Wen Huang[2,*], Lin Gu[7], and Jinxing Zhang[5,*]

[1] School of Electronic Information and Electrical Engineering, Institute of Advanced Study, Chengdu University, Chengdu 610106, China

[2] School of Integrated Circuit Science and Engineering, National Exemplary School of Microelectronics, University of Electronic Science and Technology of China, Chengdu 610054, China

[3] School of Integrated Circuits, Tsinghua University, Beijing 100084, China

[4] The College of Integrated Circuit Science and Engineering, National and Local Joint Engineering Laboratory for RF Integration and Micro-Packing Technologies, Nanjing University of Posts and Telecommunications, Nanjing 210023, China

[5] Department of Physics, Beijing Normal University, Beijing 100875, China

[6] Institute of Physics, Chinese Academy of Science, Beijing National Laboratory of Condensed Matter Physics, Beijing 100190, China

[7] School of Materials Science and Engineering, Tsinghua University, Beijing 100084, China

[#] These authors contributed equally: Junxiong Guo, Shuyi Gu, and Lin Lin

* Corresponding authors

E-mail addresses: guojunxiong@cdu.edu.cn (J.X. Guo), y-liu-17@tsinghua.org.cn (Y. Liu), uestchw@uestc.edu.cn (W. Huang), and jxzhang@bnu.edu.cn (J.X. Zhang)

Contents

Supplementary section S1. Estimation of graphene Fermi level

In this work, the graphene Fermi level was estimated by the analytical model derived as follow (ref. [S1]):

The electronic band of graphene near the Dirac point **K** can be described as:

$$E(\mathbf{k}, \pi) = \hbar v_F k \tag{S1}$$

and

$$E(\mathbf{k}, \pi) = -\hbar v_F k \tag{S2}$$

where **k**+**K** is the momentum of the Dirac Fermions, v_F is the Fermi velocity of ~1.1×10^6 m s^{-1}. According to the G phonon pattern of graphene, the band structure can be derived from the modified equation:

$$E(\mathbf{k}, \pi^*/\pi, \mathbf{u}) = \pm\hbar v_F|\mathbf{k}-\mathbf{s}(\mathbf{u})| \tag{S3}$$

where ***s*** is a vector of Dirac point shifted from K, $s = u\sqrt{2}\langle D_\Gamma^2\rangle_F$ and $\mathbf{s}\cdot\mathbf{k} = 0$, $\langle D_\Gamma^2\rangle_F = 45.6$ eV^2 $Å^{-2}$, Γ is the charged particle scattering rate. When a phonon exists, the phonon energy $\hbar\omega_{EF}$ can be determined as:

$$\hbar\Delta\omega = \hbar\omega_{E_F} - \hbar\omega_0 = \frac{\hbar}{2M\omega_0}\frac{\mathrm{d}^2\Delta E}{(\mathrm{d}u)^2} \tag{S4}$$

where E_F is the graphene Fermi energy, M is the atomic (carbon) mass, ω_0 is the frequency in undoped state, $\Delta\omega << \omega_0$, and ΔE is the variation of the electronic energy. In graphene, the G-peak position is dependent of its Fermi level, according to the experiments which breakdowns the adiabatic Born–Oppenheimer approximation, can be expressed as:

$$\Delta E(u) = \frac{4A}{(2\pi^2)}\int_{E(\mathbf{k},\pi^*,\mathbf{0})<E_F} E(\mathbf{k}, \pi^*, \mathbf{u})\mathrm{d}^2k + \mathrm{O}(u^3) \tag{S5}$$

where A is the unit cell area. Combining the eqns. S3-S5, it can be carried out the Fermi level E_F as a function of the frequency shifts as:

$$\hbar\Delta\omega = \frac{\hbar A\left\langle D_\Gamma^2\right\rangle_F}{\pi M\omega_0(\hbar v_F)^2}|E_F| = \alpha'|E_F| \tag{S6}$$

where $\alpha' = 4.39\times10^{-3}$.

Supplementary section S2. Numerical calculation for graphene dynamical conductivity

The complex conductivity of graphene σ_g can be calculated within the random-phase approximation (RPA), the dynamic optical response of graphene can be derived from Kubo formula in a complex form consisting of interband and intraband contribution, shown in eqn. S7 (refs. [S2, S3]).

$$\sigma_g = \sigma_{intra} + \sigma_{inter,1} + i\sigma_{inter,2} \tag{S7}$$

Here, the intraband conductivity of graphene σ_g follows the Drude-like model, shown in eqns. S8 and S9.

$$\sigma_{intra} = \sigma_0 \frac{4\mu_c}{\pi} \frac{1}{\hbar\tau_1 - i\hbar\omega} \tag{S8}$$

$$\sigma_0 = \frac{\pi e^2}{2h} \tag{S9}$$

where τ_1 is the relaxation rate associated with intraband transitions, and μ_c is the chemical potential of graphene, equals to the Fermi level of graphene E_F. The interband conductivity of graphene $\sigma_{inter,1}$ and $\sigma_{inter,2}$ follows the form of eqns. S10 and S11, respectively.

$$\sigma_{inter,1} = \sigma_0 \left(1 + \frac{1}{\pi} \arctan \frac{\hbar\omega - 2\mu_c}{\hbar\tau_2} - \frac{1}{\pi} \arctan \frac{\hbar\omega + 2\mu_c}{\hbar\tau_2} \right) \tag{S10}$$

$$\sigma_{inter,2} = -\sigma_0 \frac{1}{2\pi} \ln \frac{(2\mu_c + \hbar\omega)^2 + \hbar^2\tau_2^2}{(2\mu_c - \hbar\omega)^2 + \hbar^2\tau_2^2} \tag{S11}$$

where τ_2 is the relaxation rate associated with interband transitions.

Supplementary section S3. Finite element method (FEM) for electric field simulation

For our designed photodetector consisting of graphene and periodically polarized BFO strips, the near-field distribution at plasmonic resonance frequency with different Fermi levels and domain periods were simulated using FEM. Graphene was modeled using a uniaxial anisotropic permittivity assuming that the graphene layer was a surface current with non-thickness. In this model, the graphene conductivity was described using the Drude-like model (as seen in Supplementary section S2 for details). The thickness of BFO was 25 nm, corresponding to the actual epitaxial growth film. The refractive index of BFO was using a model of Kumar et al. Periodical conditions were imposed on the double sides of our simulated region. The width of our simulated region corresponds to the experimental polarization domain width, that is the simulated width varying from 100 to 500 nm; The graphene Fermi level was using the estimated results via the Raman G-peak shits. The E_F of graphene on upward and downward domains was set as +121 meV and –448 meV, respectively, according to the Raman-G band frequencies shift.

Supplementary section S4. Regulating resonance frequency by rescaling the ferroelectric domain width

In the nonretarded regime of $q << q_0$, the dielectric-graphene-dielectric architecture behaves a TM plasmon mode, and the graphene plasmon wave vector q follows eqn. S12 (ref. [S4]):

$$q \approx \frac{i2\omega\varepsilon_0\varepsilon_r}{\sigma(q,\omega)} \tag{S12}$$

where $q_0 = \omega/c$ is the incident light wave vector in free space, ω, c ε_0, and ε_r are the anglar frequency of incident light, vaccum light speed, vaccum dielectric constant, relative dielectric constant of BFO, respectively. $\sigma(q, \omega)$ is the dynamical conductivity of graphene, as well defined as σ in eqn. S7 of Supplementary section S2. For our designed device, because of the long-wavelength incident light and high-doping of graphene printed by BFO, the graphene conductivity is dominated by intraband contributions, following eqns. S8 and S9. We submit eqns S8 and S9 into eqn. S12 to achieving the graphene plasmon dispertion relation in long-wavelength region as eqn. S13 (ref. [S5]).

$$q(\omega) = \frac{2\pi\varepsilon_0\varepsilon_r}{e^2E_F}\omega^2\left(1+\frac{i}{\tau_1\omega}\right) \tag{S13}$$

To resonantly enhance the light-matter interactions, the wavevector difference between incident light wave and excited surface plasmon wave must be compensated by the periodic grating condition as eqn. S14 (ref. [S6]):

$$\mathrm{Re}\{q(\omega)\} = q_0\sin\theta \pm N\frac{2\pi}{a} \tag{S14}$$

where θ is the incident angle, and $N = 1, 2$ $N = 1, 2, 3, \ldots$, respectively. $\frac{2\pi}{a}$ represents the reciprocal vector of the grating and a is the period of grating. Therefore, we can achive the graphene plasmon resonace disperation relation as eqn. S15,

$$\omega_{spr} = \left(\frac{e^2E_F}{2\pi\hbar^2\varepsilon_0\varepsilon_r}\left(q_0 \pm N\frac{\pi}{d}\right)\right)^{\frac{1}{2}} \tag{S15}$$

where $a = 2d$, and d is the ferroelectric domain width. For the given Fermi levels of ferroelectric superdomain printing graphene, we can easily regulated the resonance frequency by rescaling the ferroelectric domain width.

Supplementary section S5. Infrared imaging simulation

The infrared imaging simulation is established to reproduce a complete physical imaging process using two types of photodetector array. As shown in Fig. S6a, the process consists of three sections, including target temperature collection, data proceesing, deep training and recognition. The target temperature were captured using a commercial camera (Melexis, 192×144 pixels). The environment temperature remains 20℃ when we collect the target temperatures.

The data processing is conducted by using an open source project called OPENZYNQ (https://github.com/openzynqhardware/openzynq). In brief, the OPENZYNQ project uses a ZYNQ7010/7020 BGA400 pin 4-layer PCB. The core board configuration mainly includes: (1) 16-bit DDR3, (2) PS and PL reset buttons, one each, (3) QSPI W25Q64/128, (4) SD card slot, (5) CH340 serial to USB converter, (6) JTAG interface, (7) USB dedicated I/O port, (8) PL with a 50MHz active crystal oscillator and PS with a 33.3MHz active crystal oscillator, and (9) automatic boot mode switching: SD card boot when an SD card is inserted, QSPI boot when not inserted. It is worth noting that, to ensure fairness in subsequent image recognition, the total number of optoelectronic detectors simulated for infrared imaging is the same in both approaches. The difference lies in the fact that in the traditional single-channel array (SCA) photodetectors, one device corresponds to one pixel, while in the multi-channel array (MCA) photodetector, 6 devices form a single pixel (see Fig. 1b in main text for details). In other words, the MCA image has one-sixth the number of pixels compared to SCA.

Supplementary section S6. Neonural network training and recognition

Figure S6b shows the artificial neural network we employed in this work. Back-propagation (BP) algorithm is used for training and recognition processes. The activation function in Hidden layer and Output layer is ReLU. The learning rate is set as a fix value 0.01. As mentioned in Supplementary section S5, the input images size of 144×192 pixels and 72×64 pixels, convolution layers of 5×5×20 and 3×3×12 for the structure of neural network within SCA and MCA-based models, respectively. The classification outputs are set as (0, 1, 2, 3, 4, 5), (0, 1), and (0, 1) in recognition of gesture shapes, curled fingers, and overlapped leaves, respectively.

Supplementary section S7. Supplementary figures

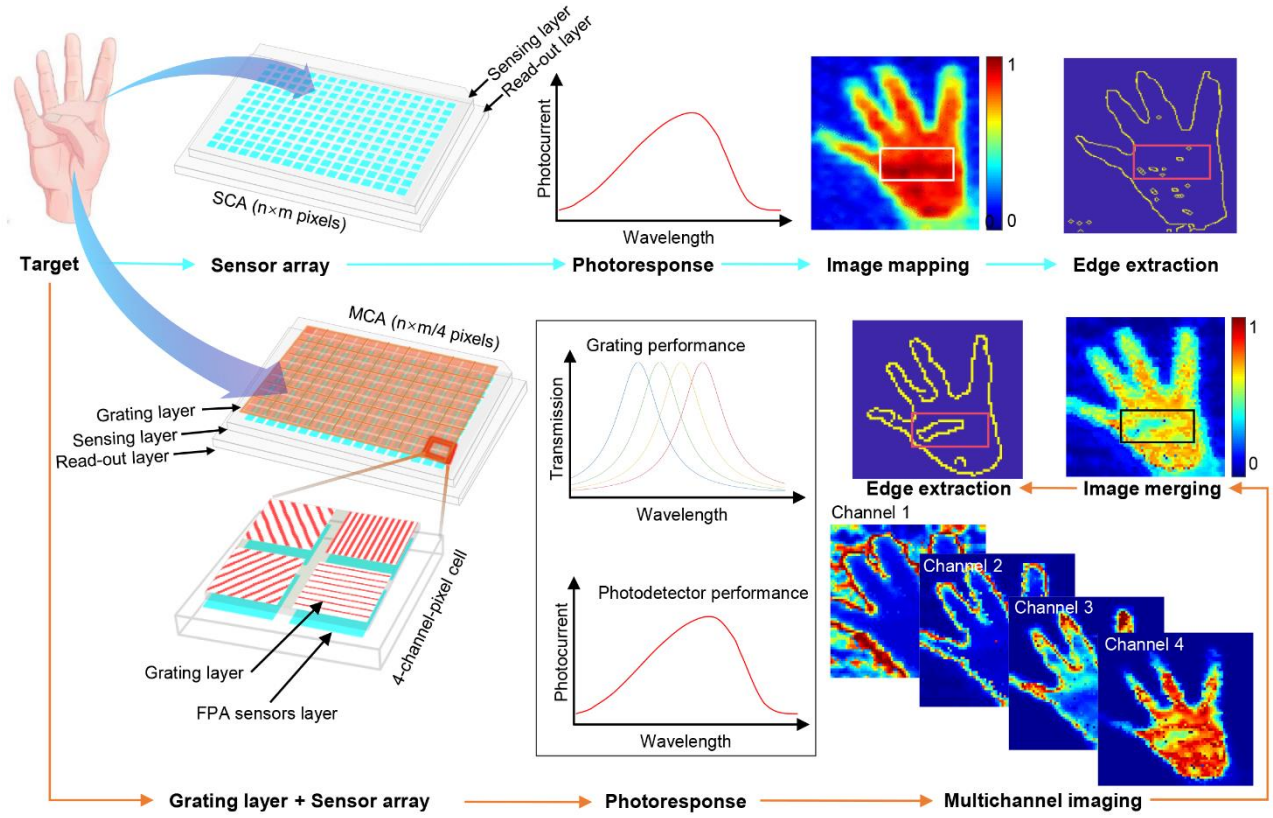

Fig. S1. Schematic of infrared imaging.

A comparison between the traditional infrared imaging approach using single-channel array (SCA) photodetectors (top panel) and the multi-channel array (MCA) photodetectors by combining focal plane array (FPA) sensors with external gratings (bottom panel). The MCA detectors-based infrared imager accurately recognize a curled thumb, whereas the conventional approach cannot.

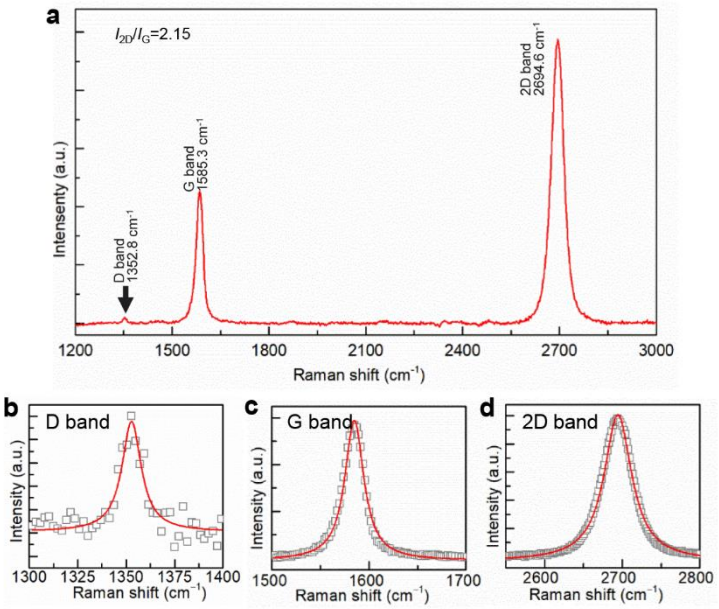

Fig. S2. **Raman characterization of graphene on pristine BFO film.**

(**a**) Raman spectrum of single-layer graphene on unpolarized BFO film. Distinct by a high 2D-to-G peak intensity ratio (I_{2D}/I_G = 2.15) and a low D band intensity, suggesting low defect density. G band positioned at 1583.5 cm^{-1} and 2D band at 2694.6 cm^{-1} indicate near-intrinsic graphene characteristics (Refs. [S7-S9]). (**b-d**) Detailed raman features of D, G, and 2D bands for graphene displayed in (**a**), with experimental data represented by gray squares and fitted curves via Lorentzian method in red.

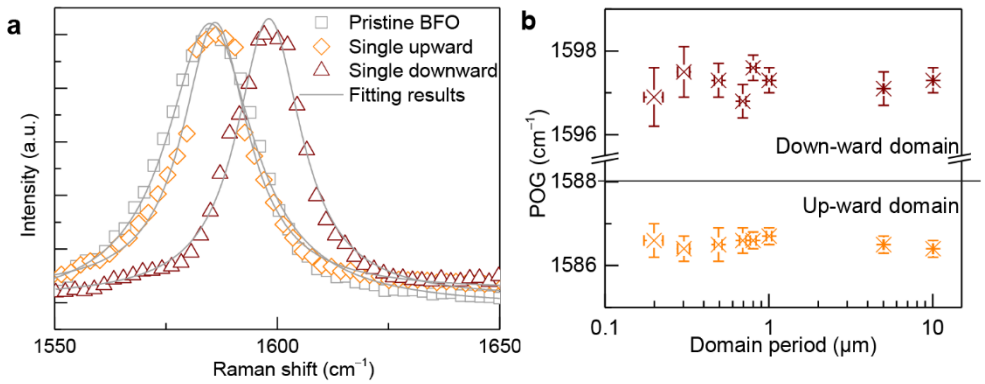

Fig. S3. Comparative Raman G-band analysis of graphene onto BFO substrate.

(**a**) Average Raman G-band frequences for graphene on fresh BFO (gray squares), single up-ward domain (orange diamonds), and single down-ward domain (wine triangles), measured at 1585.3 cm^{-1}, 1586.1 cm^{-1}, and 1597.2 cm^{-1}, respectively. Solid lines depict Lorentzian fit outcomes, confirming that graphene on up-ward domain retains near-intrinsic properties similar to the pristine BFO. (**b**) Position of graphene G-band (POG) peaks as a function of BFO superdomain period. The data are simultaneously extracted from the AFM-Raman mapping in Fig. 3b of main text. The POG peaks for graphene on up- and down-ward domains were around 1586 and 1597 cm^{-1}, respectively, confirming the feasibility of spatial printing of graphene carrier density without patterning of graphene sheet.

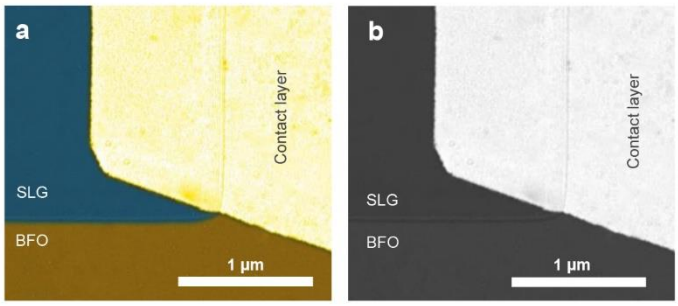

Fig. S4. SEM images for graphene/BFO-based photodetector.

(**a**) Enhanced contrast SEM image with graphene highlighted with fake-color in orange. (**b**) Raw SEM image.

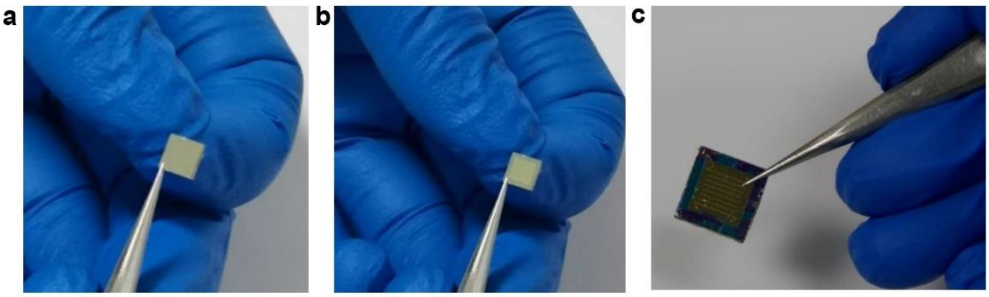

Fig. S5. Overall optical images of fabricated devices.

(**a**) Bare BFO film epitaxially grown on an STO substrate with an LSMO coating layer. (**b**) Completed device of transferred graphene onto BFO film. Sample dimensions in (**a**) and (**b**) are 5 mm × 5 mm designed for optical measurements, including Raman, transmission performances. (**c**) The assembled photodetector array featuring graphene/BFO active layers complemented by Ti/Pd/Au contact layers. The sample size in (**c**) is 10 mm × 10 mm, which accommodates additional photodetector cells to facilitate photoelectric performance assessments.

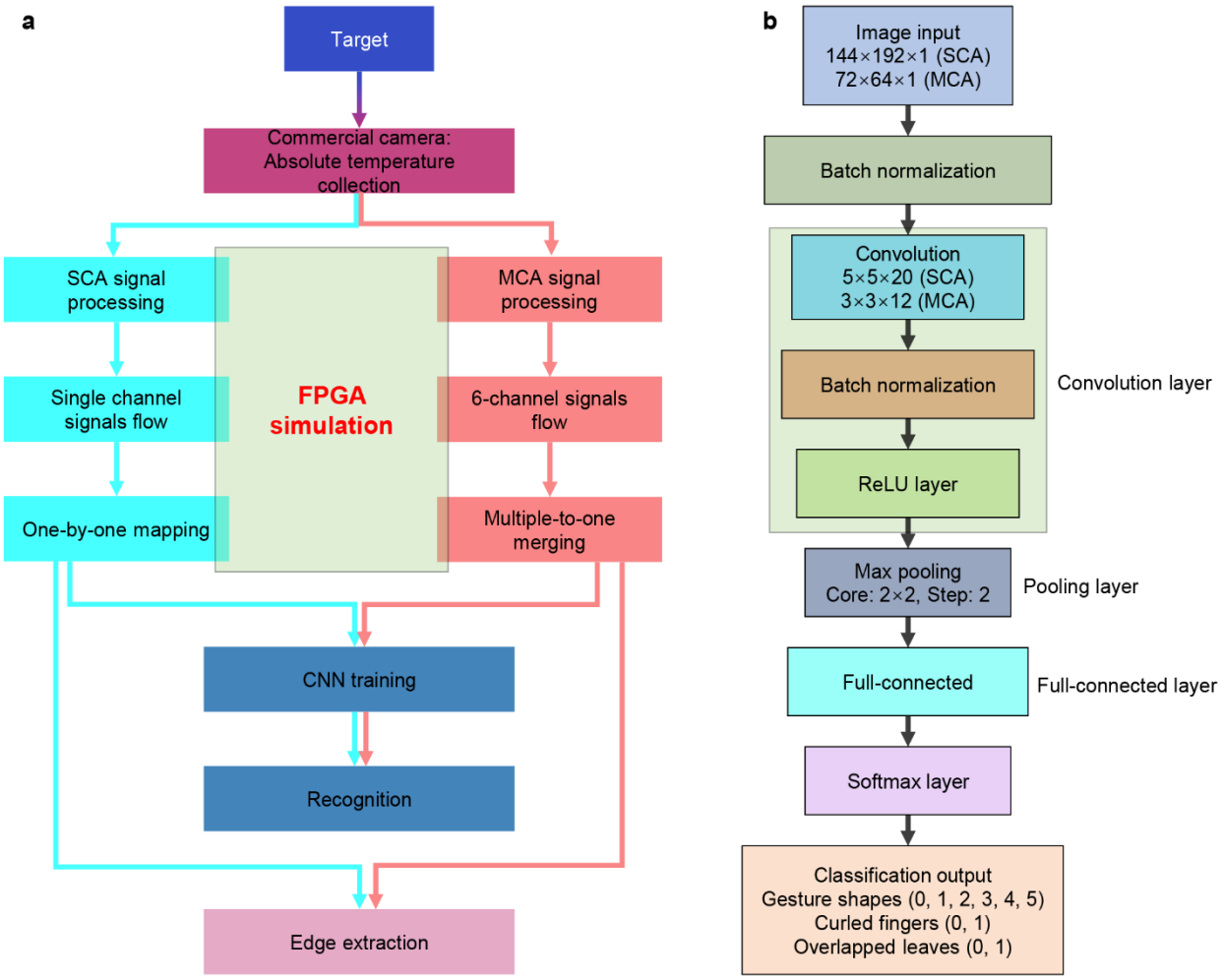

Fig. S6. Schematic of infrared imaging workflow herein.

(**a**) Overall process for deeping imaging. (**b**) Deep learning and recognition process.

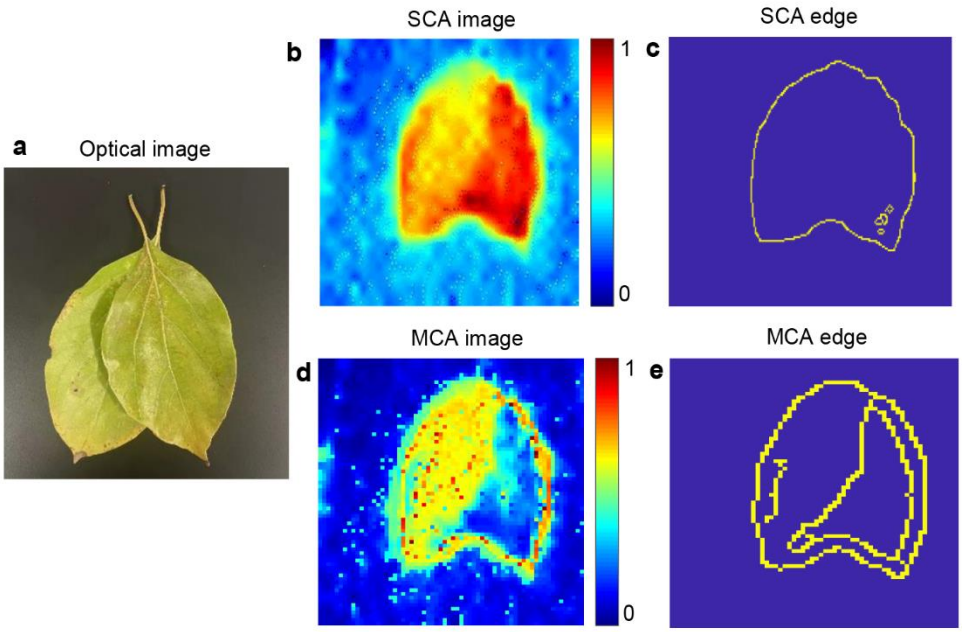

Fig. S7. Infrared imaging comparison of overlapping leaves.

(**a**) Standard optical image. Infrared snapshots (**b, d**) alongside associated edge profiles (**c, e**) for partially covered leaves using both single- and multi-channel photodetector arrays.

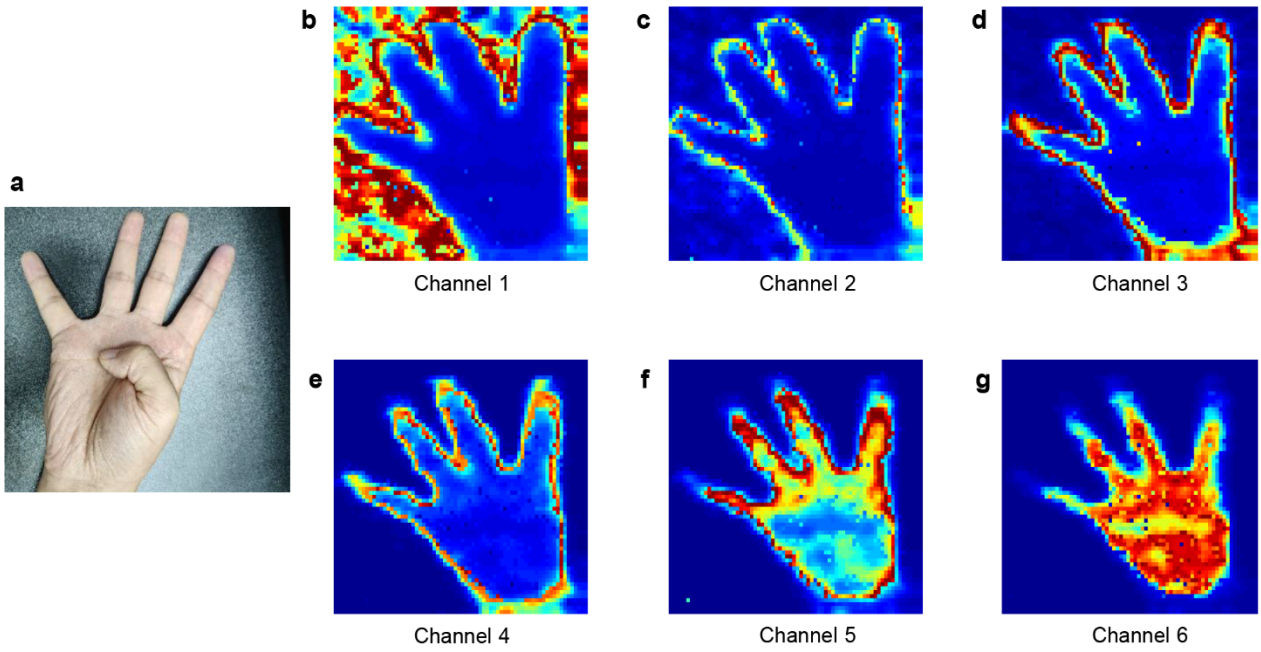

Fig. S8. Meta-infrared-imaging with multi-channel signals for curled gesture.

(**a**) Optical image of gesture 4. (**b-g**) Channel-by-channel simulation results for the proposed 6-channel model.

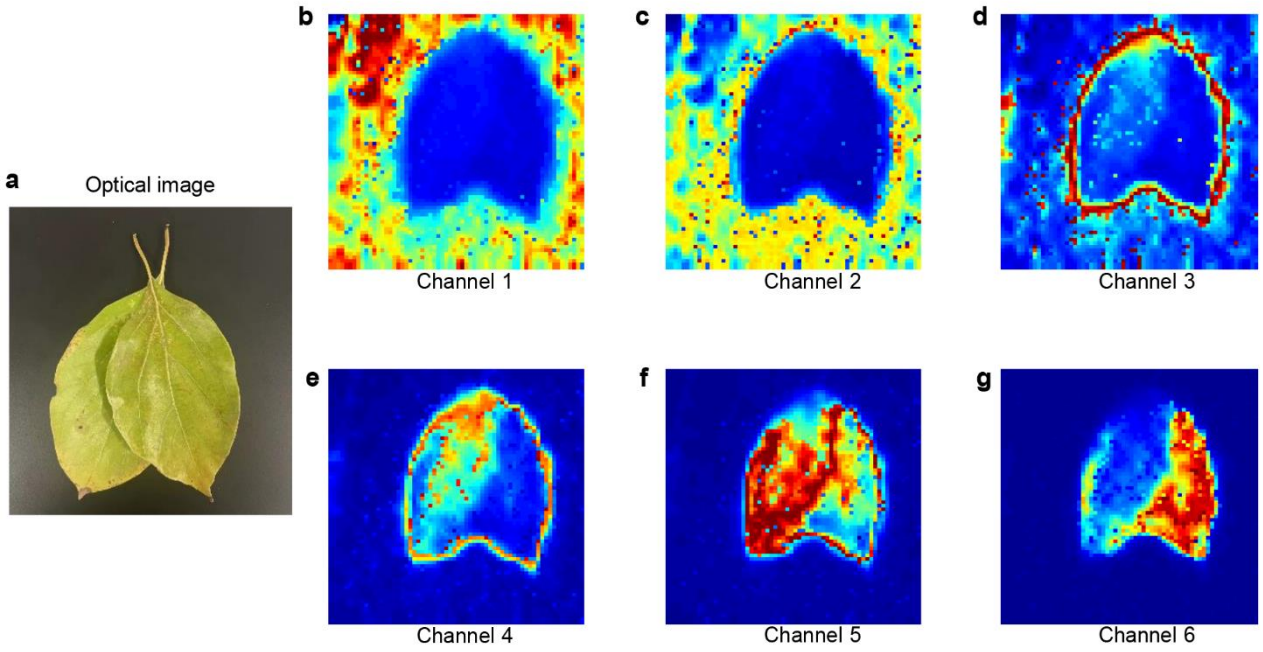

Fig. S9. Meta-infrared-imaging with multi-channel signals for overlapped leaves.

(**a**) Optical image of two intersecting leaves. (**b-g**) Multi-channel-specific simulated signals for the proposed 6-channel configuration.

Supplementary references

S1. Pisana, S. et al. Breakdown of the adiabatic Born-Oppenheimer approximation in graphene. Nat Mater 6, 198-201 (2007).

S2. Hwang, E. H., Das Sarma, S. Dielectric function, screening, and plasmons in two-dimensional graphene. Phys Rev B. 75, 6 (2007).

S3. Stauber, T. Plasmonics in Dirac systems: from graphene to topological insulators. J Phys-Condens Mat 26, 123201 (2014).

S4. Barnes, W. L., Dereux, A., Ebbesen, T. W. Surface plasmon subwavelength optics. Nature 424, 824-830 (2003).

S5. Low, T., Avouris, P. Graphene plasmonics for terahertz to mid-infrared applications. Nano Lett 8, 1086-11101 (2014).

S6. Maier, S.A. *Plasmonics: fundamentals and applications*, Springer Science & Business Media (2007).

S7. Ferrari A.C., Basko D.M. Raman spectroscopy as a versatile tool for studying the properties of graphene. Nat Nanotechnol 8, 235-246 (2013).

S8. Ferrari A.C., et al. Raman spectrum of graphene and graphene layers. Phys Rev Lett 97, 187401 (2006).

S9. Das A., et al. Monitoring dopants by Raman scattering in an electrochemically top-gated graphene transistor. Nat Nanotechnol 3, 210-215 (2008).